Formation mechanisms of embedded wurtzite and zincblende indium nitride nanocrystals

A. W. Wood, X. Weng, Y. Q. Wang, and R. S. Goldman

Additional information on Appl. Phys. Lett.
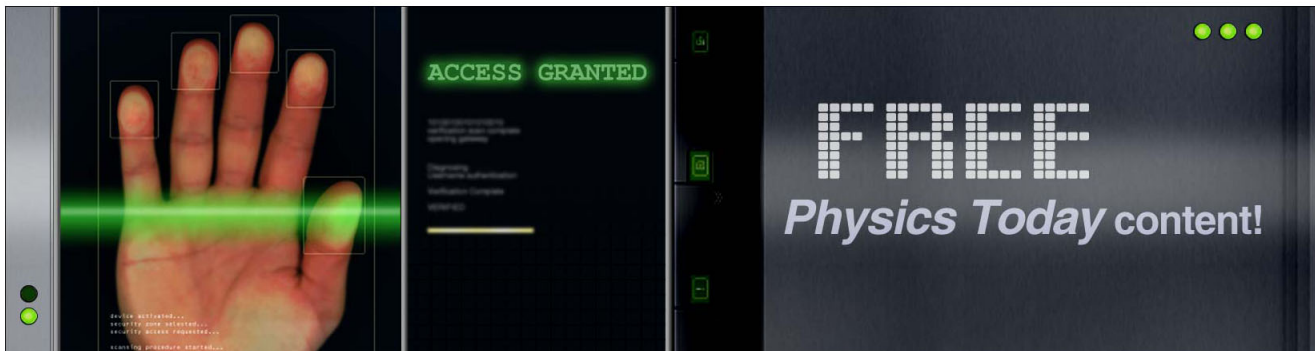
Formation mechanisms of embedded wurtzite and zincblende indium nitride nanocrystals

A. W. Wood,[1] X. Weng,[2] Y. Q. Wang,[3] and R. S. Goldman[1,4,a]

[1]*Department of Physics, University of Michigan, Ann Arbor, Michigan 48109, USA*
[2]*Materials Research Institute, Pennsylvania State University, University Park, Pennsylvania 16802, USA*
[3]*Materials Science and Technology Division, Los Alamos National Lab, Los Alamos, New Mexico 87545, USA*
[4]*Department of Materials Science and Engineering, University of Michigan, Ann Arbor, Michigan 48109, USA*

We have examined the formation of InN nanocrystals embedded in InAs. Low temperature (77K) N ion implantation into InAs leads to the formation of an amorphous layer with crystalline InAs remnants. Rapid thermal annealing up to 550 °C leads to the nucleation of zincblende InN nanocrystals with a maximum likelihood radius of 1.3 ± 0.2 nm. Rapid thermal annealing at 600 °C leads to nucleation of zincblende and wurtzite InN, with an increase in maximum likelihood radius to 2.6 ± 0.4 nm. These results are consistent with the predictions of a thermodynamic model for the nanoscale-size-dependence of zincblende and wurtzite InN nucleation. © *2011 American Institute of Physics*. [doi:10.1063/1.3617464]

Due to its low electron effective mass,[1] high electron mobility,[2] and high room temperature drift velocity,[3] InN is perhaps the most promising group III-N material for solid-state devices including long-wavelength light-emitters and detectors. Recently, interest in InN has been renewed due to reports of a low bandgap energy of 0.65-0.8 eV (Refs. 4 and 5) in lieu of the previously accepted value of 1.7-2.2 eV for wurtzite (WZ) InN.[6,7] Interestingly, the band gap of zincblende (ZB) InN is predicted to be 0.58 eV,[8] slightly below that of WZ InN, providing an opportunity for extending nitride-based light-emitting diodes (LEDs) to the near infrared.

ZB InN formation has been reported in 2D crystals[9–11] and nanowires.[12] InN nanostructures have been produced by metal-organic vapor-phase epitaxy (MOVPE), but these structures suffer from instabilities at ambient conditions, resulting in a gradual WZ to ZB phase transformation and the formation of group-III oxides.[13] Ion beams have been used to nucleate embedded WZ and ZB InN nanocrystals using N implantation into InP (Ref. 14) and In and N co-implantation into Si,[15] respectively. Although N implantation into InAs has been examined,[16] the formation of InN nanocrystals embedded in InAs and the conditions for selective formation of ZB vs. WZ InN phases have not been reported. Therefore, we have examined the formation of embedded InN nanocrystals using ion-beam-synthesis of InAs:N, similar to matrix-seeded growth[16] of GaN nanostructures. For our lowest rapid thermal annealing (RTA) temperatures, ZB InN nanocrystals are observed. As the RTA temperature is increased, the average nanocrystal size increases, and the formation of larger nanocrystals with WZ structure is consistent with the predictions of a thermodynamic model for the nanoscale-size-dependence of nucleation of ZB and WZ InN.[17]

For these investigations, epitaxial InAs films were broad-area implanted using 100 keV N ions, with a nominal fluence of 5×10^{17} cm^{-2}. To minimize channeling effects during implantation, a 7° angle of incidence with respect to the sample surface normal was used. During implantation, the substrate temperature was maintained at 77 K. Following implantation, the samples were rapid thermal annealed in argon gas for 30 s at 500 °C, 550 °C, or 600 °C. Cross-sectional transmission electron microscope (TEM) specimens were prepared using conventional mechanical polishing, followed by argon ion milling at 77 K. TEM imaging and selected-area electron diffraction (SAD) were carried out in a JEOL 3011 operating at 300 kV, using apertures which select regions with ~ 0.10 μm diameters. Dark-field images were obtained using the InAs {220} polycrystalline ring and, in some cases, the ZB InN {111} polycrystalline reflection. We note that WZ InN reflections were too weak for dark-field imaging. All SAD patterns were calibrated to the InAs substrate {110}. Energy Dispersive X-Ray Spectroscopy (EDX) and high-angle annular dark field (HAADF) scanning transmission electron microscope (STEM) imaging were performed in a JEOL 2010 TEM operating at 200 kV.

Figure 1(a) presents a typical cross-sectional HAADF STEM image following implantation and RTA. The cavities, labeled with circles, are likely remnants of coalesced N gas bubbles at the depths of highest N concentration, similar to earlier reports of GaAs:N.[18] To determine the depth distribution of N, we assume a uniform sample thickness and estimate a Cliff-Lorimer factor from EDX data collected in regions of pure InAs, typically at 250 to 300 nm depths below the surface. A line-cut of EDX data from the surface to a depth of 300 nm reveals that the N atomic % is highest in the top ~ 50 nm of the surface (Fig. 1(b)). For depths >50 nm, the N atomic % is negligible, indicating that after RTA, N incorporation is limited to the surface layer. Thus, any N originally below the surface layer has likely segregated and agglomerated at implantation-induced defects, forming gas bubbles, as discussed elsewhere.[18]

Figure 2 presents dark-field TEM images showing an overview of InAs:N (a) as-implanted and following RTA at (c) 500 °C, (e) 550 °C, and (g) 600 °C. Most of the TEM
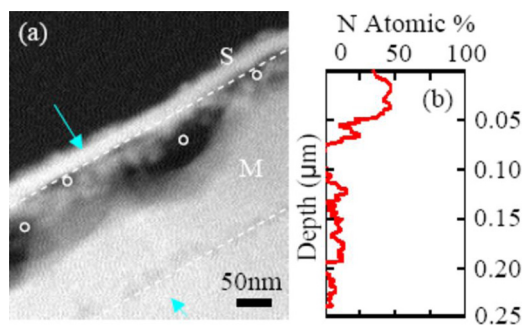
FIG. 1. (Color online) (a) Cross-sectional HAADF STEM image of a typical implanted-plus-RTA sample with a nanocrystal-rich surface layer (S) and crystalline middle layer (M). Popped N_2 gas bubbles are labeled with circles. Using the line-cut indicated in (a), the atomic ratio for N is presented in (b).

images show evidence of two layers: (1) a surface layer that increases in thickness with annealing temperature and (2) a crystalline middle layer with extended twinning, consistent with the HAADF STEM image presented in Fig. 1. The corresponding SAD patterns, shown in Figs. 2(b), 2(d), 2(f), and 2(h), respectively, indicate that RTA induces the formation of randomly oriented grains within the surface layer. During annealing of the implanted layer, there is a competition between nanocrystal nucleation at the surface and InAs recrystallization near the substrate. For high temperature RTA, nanocrystal nucleation dominates and the surface layer expands. For low temperature RTA, recrystallization of the InAs dominates, and instead the near-substrate layer expands.

For as-implanted InAs:N, the dark-field TEM image presented in Fig. 2(a) reveals a 200 nm thick amorphous surface layer. The SAD pattern collected from the surface layer (Fig. 2(b)) exhibits diffuse rings, confirming significant damage in the surface layer. However, high resolution TEM (HRTEM) images of the interface between the damaged layer and the host InAs matrix (Fig. 3(a)) indicate the presence of an amorphous matrix with remnants that have maintained the structure of crystalline InAs.

Following RTA at 500 °C, dark-field TEM imaging, presented in Fig. 2(c), reveals two layers: a 20–30 nm polycrystalline surface layer and a crystalline middle layer with extended defects. In the surface layer, bright spots indicate the formation of embedded nanocrystals separated by 5–20 nm. Both the crystallite formation and N incorporation appear to be confined to the surface layer, indicating that N incorporation is limited to the nanocrystals embedded in the surface. SAD collected from both the surface and middle layers is shown in Fig. 2(d). The diffraction spots are likely associated with misaligned InN nanocrystals within the surface layer. HRTEM of the nanocrystal region (Fig. 3(b)) indicates crystallite lattice parameters of 2.95 and 2.59 Å, within 4.8% of the {111} and {200} interplanar spacings of ZB InN.

Figures 2(e) and 2(g) present dark-field TEM images of InAs:N following RTA at 550 °C and 600 °C, respectively. For 550 °C (600 °C) RTA, the thickness of the polycrystalline surface layer has increased from 20–30 nm to a thickness of ~50 nm (~80 nm). The corresponding HRTEM image from the vicinity of the surface-middle layer interface following 550 °C RTA is shown in Fig. 3(c). The middle layer is crystalline with extended defects, while the surface layer consists of randomly oriented nanocrystals. SAD and HRTEM
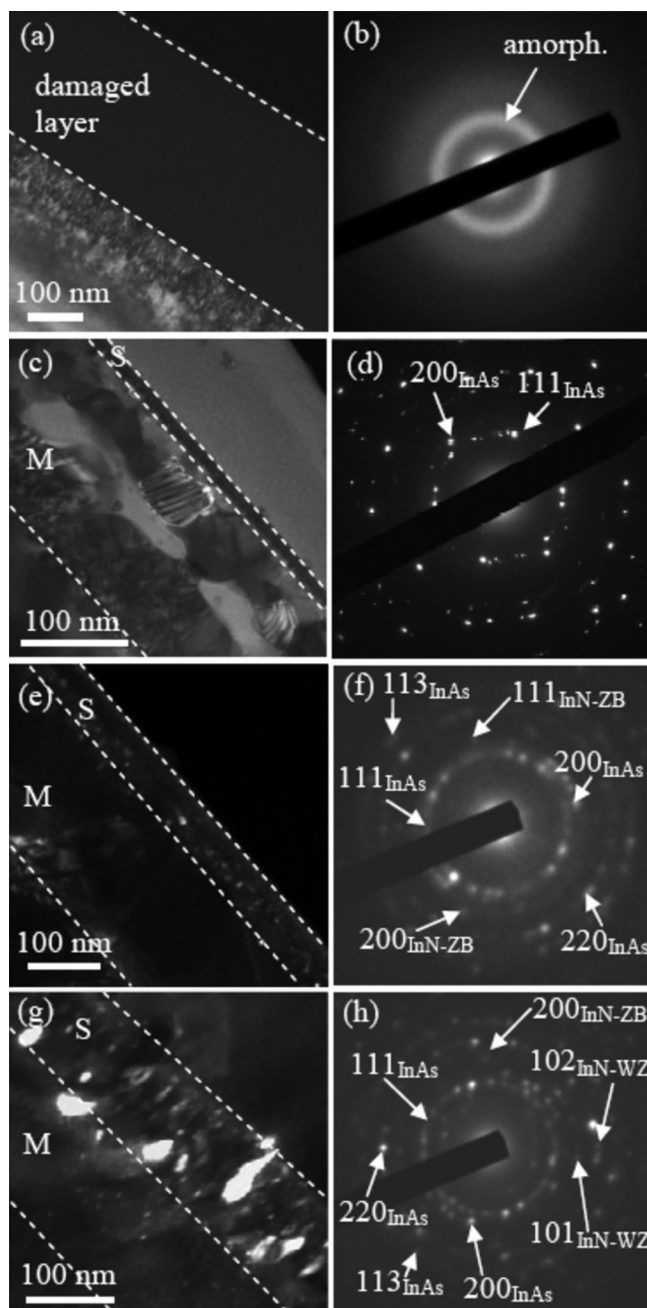

FIG. 2. Dark-field TEM images of (a) as-implanted InAs:N layers and InAs:N layers following RTA at (c) 500 °C, (e) 550 °C, and (g) 600 °C. The corresponding SAD patterns, collected from the damaged layer of (a) and surface (S) layer of (c), (e), and (g), are presented in (b), (d), (f), and (h), respectively.

imaging indicate a density of twinning in the nanocrystals $<19.4\ \mu m^{-2}$.

Nanocrystal identification using SAD and HRTEM collected from the surface layers is presented in Figs. 2(f) and 2(h) and Figs. 3(d)–3(f). Comparisons of the interplanar spacings measured by SAD with powder diffraction standards are shown in Table I.[19] For RTA at 550 °C, d-spacings of 2.85 and 2.48 Å are observed, corresponding to ZB InN. For RTA at 600 °C, d-spacings of 3.03, 2.59, 2.40, and 2.10 Å are apparent, within 3 to 4% of the {100} and {101} interplanar spacings of WZ InN, the {200} interplanar spacing of ZB InN, and the {102} interplanar spacing of WZ InN. These distortions are significantly lower than the 39% (22%)
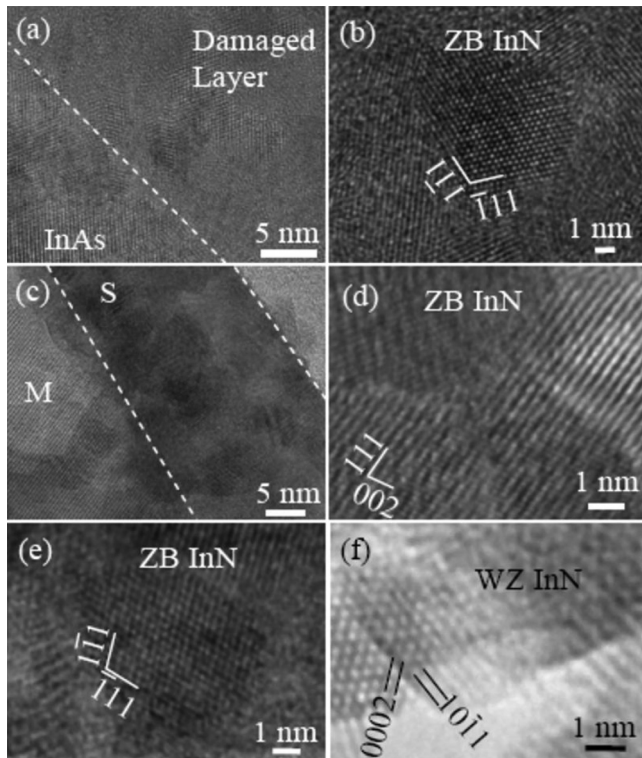
FIG. 3. HRTEM images of InAs:N layers (a) as-implanted and following RTA at (b) 500 °C, (c,d) 550 °C, and (e,f) 600 °C. For (a) the as-implanted layers, there are remnant InAs grains in an amorphous matrix near the substrate. Following RTA at (b) 500 °C and (c,d) 550 °C, nanostructures with lattice parameters similar to ZB InN, within an amorphous matrix, are apparent in the surface layers (S). Following RTA at 600 °C, both (e) ZB InN and (f) WZ InN nanocrystals have nucleated within the S layer.

TABLE I. Interplanar spacings of InAs:N following RTA at 550 °C and 600 °C measured by SAD, in comparison to powder diffraction standards.[19]

d-Spacing (Å) (experimental)		Powder diffraction standard (Å)		
550 °C RTA	600 °C RTA	ZB InN (hkl)	WZ InN (hkl)	InAs(hkl)
3.47	3.50			3.50 (111)
3.02	3.03		3.06 (100)	3.03 (200)
2.85		2.86 (111)	2.85 (002)	
	2.59		2.69 (101)	
2.48	2.40	2.47 (200)		
2.13	2.16			2.14 (220)
	2.10		2.09 (102)	
1.82	1.82			1.83 (113)

Therefore, we assume an unstrained spherical solid nucleating from a liquid. We use the radial dependence of the InN surface energy, σ_{InN}, to estimate the size-dependence of the free energy for nucleation of ZB and WZ InN. The resulting difference in free energies, ΔG_{ZB}-ΔG_{WZ}, as a function of nanocrystal radius, is presented in Ref. 17. For 600 °C (550 °C) RTA, ZB InN is favored when r < 6.25 Å (6.50 Å). For larger r, WZ InN is favored, consistent with literature reports for the relative stability of bulk WZ vs. ZB InN.[20] Indeed, with an increase in RTA temperature to 600 °C, the average nanocrystal size has increased, and both ZB and WZ InN nanocrystals are apparent. For small r, the reduction in free energy of the ZB phase in comparison with that of the WZ structure is driven by a minimization of σ_{InN}. Indeed, σ_{InN} is minimized by adoption of the ZB crystal structure, which has a higher density of low energy {111} surface planes in comparison with that of the WZ structure.

distortion for WZ (ZB) InN nanocrystals coherent with InAs, suggesting the formation of semi-coherent InAs/InN interfaces. The {002} reflection of WZ InN is likely missing due to the low density of WZ InN grains, as evidenced by the spotty rings of SAD in Fig. 2(h). WZ InN nucleation is further supported by the fact that the 2.59 and 2.10 Å rings lie between the {111} and {200} ZB InN reflections and the {220} and {113} InAs reflections, respectively.

The nucleation of InN nanocrystals is confirmed by HRTEM studies (Fig. 3(d)–3(e)), which reveal average lattice fringe spacings of 2.89 and 2.53 Å, within 2.4% of the {111} and {200} interplanar spacings of ZB InN. In addition, for the nanocrystals in Fig. 3(f), the average lattice fringe spacings are 2.83 and 2.61 Å, within 3.3% of the {002} and {101} interplanar spacings of WZ InN.

To consider the effect of nanocrystal nucleation size on the formation of WZ vs. ZB InN, a distribution of nanocrystal sizes, estimated from several dark-field TEM images, is presented in Ref. 17. We fit the size distributions with a Poisson log-normal regression for nanocrystal nucleation frequency as a function of radius and use the maximum likelihood estimation method to calculate the most probable nanocrystal radius. With increasing RTA temperature, the nanocrystal size increases from 1.3 ± 0.2 nm (550 °C RTA) to 2.6 ± 0.4 nm (600 °C RTA). We use a thermodynamic model to consider the influence of nanocrystal size on the nucleation of ZB and WZ InN.[17] The crystallites form in an amorphous matrix; thus, strain is not expected to play a role in their nucleation.

[1]J. Wu *et al.*, Phys. Rev. B **66**, 201403 (2002).
[2]V. W. L. Chin, T. L. Tansley, and T. Osotchan, J. Appl. Phys. **75**, 7365 (1994).
[3]S. K. O'Leary *et al.*, J. Appl. Phys. **83**, 826 (1998).
[4]V. Yu. *et al.*, Phys. Stat. Sol. B **230**, R4 (2002).
[5]J. Wu *et al.*, Appl. Phys. Lett. **80**, 3967 (2002).
[6]N. Puychevrier and M. Menoret, Thin Solid Films **36**, 141 (1976).
[7]K. L. Westra and M. J. Brett, Thin Solid Films **192**, 227 (1990).
[8]F. Bechstedt *et al.*, Phys. Stat. Sol. (a) **195**, 628 (2003).
[9]C. L. Hsiao *et al.*, Appl. Phys. Lett. **92** 111914 (2008).
[10]J. G. Lozano *et al.*, Appl. Phys. Lett. **90**, 091901 (2007).
[11]X. Xu *et al.*, Appl. Phys. Lett. **87**, 092102 (2005).
[12]C. Nie *et al.*, Chin. Phys. Lett. **25**, 1780 (2008).
[13]D. González *et al.*, J. Appl. Phys. **105**, 013527 (2009).
[14]K. Santhakumar *et al.*, Nucl. Inst. Meth. Phys. Res. B **212**, 521 (2003).
[15]Y. K. Huang *et al.*, Appl. Phys. Lett. **91**, 091921 (2007).
[16]X. Weng *et al.*, J. Appl. Phys. **97**, 064301 (2005).
[17]See supplementary material at http://dx.doi.org/10.1063/1.3617464 for details of size distribution and thermodynamic model for nucleation of ZB and WZ InN nanocrystals.
[18]X. Weng *et al.*, J. Vac. Sci. Technol. B **22**, 989 (2004).
[19]International Centre for Diffraction Data: Newtown, PA, 2005; PDF#00-015-0869, PDF#04-012-6448, PDF#00-050-1239 (accessed Feb 15, 2011).
[20]M. Leszczynski, in *Properties, Processing and Applications of Gallium Nitride and Related Semiconductors*, edited by J. H. Edgar, S. T. Strite, I. Akasaki, H. Amano, and C. Wetzel (INSPEC, London, UK, 1999), p. 3.